Front. Struct. Civ. Eng. 2022, 16(3): 359–377
https://doi.org/10.1007/s11709-022-0816-2

RESEARCH ARTICLE

A study on bearing characteristic and failure mechanism of thin-walled structure of a prefabricated subway station

Lianjin TAO[a], Cheng SHI[a], Peng DING[b,c*], Sicheng LI[a], Shang WU[a], Yan BAO[a]

[a] *Key Laboratory of Urban Security and Disaster Engineering of the Ministry of Education, Beijing University of Technology, Beijing 100124, China*

[b] *Department of Hydraulic Engineering, Tsinghua University, Beijing 100084, China*

[c] *China Construction Science & Technology Group Co., Ltd, Beijing 100195, China*

[*] *Corresponding author. E-mail: dingpeng20@tsinghua.org.cn*

ABSTRACT In order to study the bearing performance of a new type of prefabricated subway station structure (PSSS), firstly, a three-dimensional finite element model of the PSSS was established to study the nonlinear mechanics and deformation performance. Secondly, the bearing mechanism of a PSSS was investigated in detail. Finally, the development law of damages to a thin-walled prefabricated component and the failure evolution mechanism of a PSSS were discussed. The results showed that this new type of the PSSS had good bearing capacity. The top arch structure was a three-hinged arch bearing system, and the enclosure structure and the substructure were respectively used as the horizontal and vertical support systems of the three-hinged arch structure to ensure the integrity and stability of the overall structure. Moreover, the tongue-and-groove joints could effectively transmit the internal force between the components and keep the components deformed in harmony. The rigidity degradation of the PSSS caused by the accumulation of damages to the spandrel, hance, arch foot, and enclosure structure was the main reason of its loss of bearing capacity. The existing thin-walled components design had significant advantages in weight reduction, concrete temperature control, components hoisting, transportation and assembly construction, which achieved a good balance between safety, usability and economy.

KEYWORDS prefabricated subway station, thin-walled components, finite element analysis, bearing characteristic, failure mechanism

1 Introduction

Prefabricated construction technology (PCT) is an important advance in building industrialization, which has broad application prospects and deep development potential [1–4]. Compared with traditional cast-in-place (CIP) construction technology, PCT has a series of advantages [5–12], such as fast construction speed, convenient construction, no formwork and CIP concrete work, less construction disturbance, reducing material and energy waste, small labor demand, high degree of mechanized construction, high industrial production efficiency, high quality assurance rate, good economic and social environmental benefits. Therefore, with the continuing urbanization, considerable progress has been made in infrastructure construction capabilities in China [13,14], and the inherent advantages of PCT have once again aroused great interest in academic and engineering circles; PCT has gradually been promoted to the construction of underground structures.

Russia, the Netherlands, France, Japan, and other countries have used PCT in underground projects and have achieved many research results [15,16]. For example, the United States successfully constructed an underground fuel depot using PCT in 1985 [17]; Russia built an Olympic subway station using a prefabricated single-arch

Article history: Received Jun 23, 2021; Accepted Dec 18, 2021

structure in 1996 [18]; Tokyo, Japan, built an underground reservoir using prefabricated concrete beam technology in 1998 [19]; the University of Minnesota in the United States built an underground library using prefabricated concrete circular slabs in 2000 [20]. Until the present, the PCT has mainly been used in the construction of tunnels by the shield method and underground comprehensive pipe corridors with smaller dimensions in China's underground engineering. Chinese scholars [21–24] have carried out a lot of research work on the design of shield segments, the performance of segment joints, and the seismic design of shield tunnels. However, the application and research of PCT in large underground structures is still in its infancy. The Yuanjiadian (later renamed Shuangfeng) Station [25–27] of Changchun Rail Transit Line 2 was the first large-scale subway station constructed with PCT in China. After successful application in several stations in Changchun, it has gradually been applied in subway station construction in Qingdao and Shenzhen. Ding et al. [28–30], Tao et al. [31,32], and Li et al. [33–35] studied the overall performance of prefabricated subway station structures (PSSS) and the mechanical properties of the tongue-and-groove joints of the PSSS, respectively. Studies showed that the PSSS had good integrity, and the joints had good mechanical properties. The seismic performance of the PSSS was basically equivalent to that of the CIP structure under design and rare earthquake conditions. Furthermore, the Jin'anqiao Station [36–39] on Beijing Subway Line 6 was constructed with an integral assembly structure. Precast concrete square piles were used to construct the enclosure structure in the deep and large foundation pit project of the Yanmazhuang West Station [40] of Jinan Rail Transit Line 1. The Wuzhong Road Station [41] of Shanghai Subway Line 15 adopted the construction technology of large-span column-free subway station with prefabricated assembly combined with CIP superimposed arch shell, which could effectively speed up the construction progress. In order to meet the lightweight requirements in the process of prefabricated component production, hoisting and transportation, and on-site assembly, and to optimize the mechanical properties of the prefabricated structure, many scholars proposed a research idea of combining PCT with hollow structure. The intention has been to offer innovation and environmental protection through experimental analysis and theoretical research on prefabricated structures. For example, Chu et al. [42] and Xiong et al. [43] studied and compared the mechanical behaviors of precast hollow shear wall and CIP shear walls through quasi-static experiments. Studies showed that the shear behavior of precast hollow shear wall was slightly lower than that of CIP shear wall, but the ductility and hysteretic energy of the precast hollow shear wall were better than those of the CIP shear wall. Gu et al. [44] compared the seismic performance of double-face superposed shear wall and CIP shear wall and found that the mechanical properties of the precast hollow shear wall under cyclic loading were similar to those of the CIP shear wall. Furthermore, the floors and roofs assembled from prestressed hollow slabs in modern industrial buildings also had better bending and shear resistance, and had many advantages compared with traditional concrete components, such as better quality-control, lower on-site labor cost and shorter construction time [45–47]. Cases of combining PCT with hollow structures also included prefabricated hollow slab bridges [48–50], prefabricated hollow piers [51,52], prefabricated hollow stairs [53], and so on. When the prefabricated structure adopted a reasonable hollow type, it could reduce the self-weight of the structure while ensuring the bearing capacity and integrity of the structure, reduce the project cost, and speed up the construction speed.

In summary, scholars have carried out extensive and in-depth research on prefabricated structures, have performed beneficial explorations on the process of combining PCT with hollow structures, and have made many attempts to research underground prefabricated structures. However, there have been few reports on the design of the large-scale PSSS using hollow weight-reduction technology with thin-walled closed-cavity components. The research problems of this new type of PSSS can be summarized as follows. 1) The bearing characteristics of PSSS are still unclear. 2) Research on the mechanics and deformation properties of PSSS is lacking. 3) Research on the failure mechanism of PSSS under ultimate bearing condition is still relatively scarce. Therefore, it is urgent to carry out systematic and in-depth research. The research results will have important scientific research significance and construction reference value for giving full opportunity to take advantage of PCT and hollow weight-reduction technology, for tapping the energy-saving and efficiency-increasing potential of the prefabricated structure, and for optimizing the design and construction of the prefabricated structure.

This paper mainly studies the bearing characteristics and failure law of the single-ring thin-walled PSSS in Changchun. The outline of the article is as follows. Section 2 introduces the background of the engineering problem and summarizes the basic situation of PSSS. In Section 3, the establishment of the three-dimensional (3D) finite element model (FEM) of the PSSS, the selection of the constitutive model and related parameters, and the loading calculation conditions are described. In Section 4, the calculation results are analyzed, including mechanical properties, deformation performance, bearing mechanism and failure mechanism. Section 5 discusses the advantages and disadvantages of using thin-walled closed-cavity types for structural components of large underground PSSS. Section 6 contains the conclusions and a summary of the paper.

2 Engineering background

Rail Transit Line 2 in Changchun City, Jilin Province, China opened for operation on August 30, 2018. Five of the stations were built with PCT, namely: West Lake Station, Shuangfeng Station, Xinglongpu Station, West Ring Road Station and Jianshe Square Station, as shown in Fig. 1(a). These stations have been in safe operation for more than 3 years. The traditional technology in the construction of subway stations, such as steel bar processing, template making, concrete pouring, etc., has been transformed into industrialized mass production of components in the prefabricated component factory, adopting the flow operation mode. Then, according to the requirements of the construction schedule of the subway station, the qualified prefabricated components are transported to the station construction site for assembly operations in a timely manner, which can greatly improve the efficiency and flexibility of the subway station construction, as shown in Fig. 1(b). The PCT is not affected by the weather and severe cold seasons, effectively shortens the construction period, greatly reduces the impact of construction on the surrounding environment, and has broad application prospects and market value. At present, 15 subway stations in the planned (under construction) line of Changchun Rail Transit continue to be constructed using PCT. In addition, Qingdao Metro Line 6 and Shenzhen Metro Line 16 are planned (under construction) to have 6 and 3 subway stations constructed using this PCT, respectively.

3 Numerical model

3.1 Finite element model

The PSSS system mainly consists of the prefabricated structure and the enclosure structure. The longitudinal width of each standard ring of the prefabricated structure is 2 m. The standard ring is composed of seven prefabricated components of five types, including base plate A, B (left BL, right BR), side wall C (left CL, right CR), top arch D, E blocks. The supporting facilities such as middle plate, middle column and bottom beam are constructed by

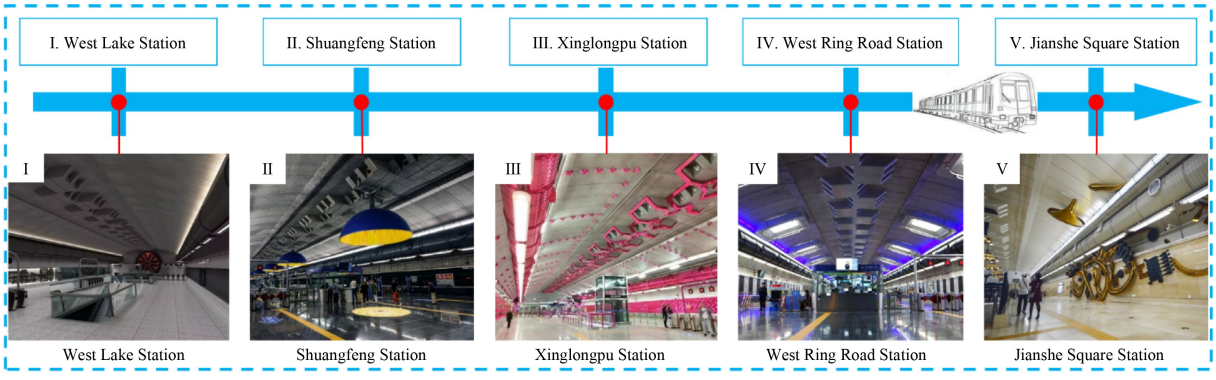

(a)

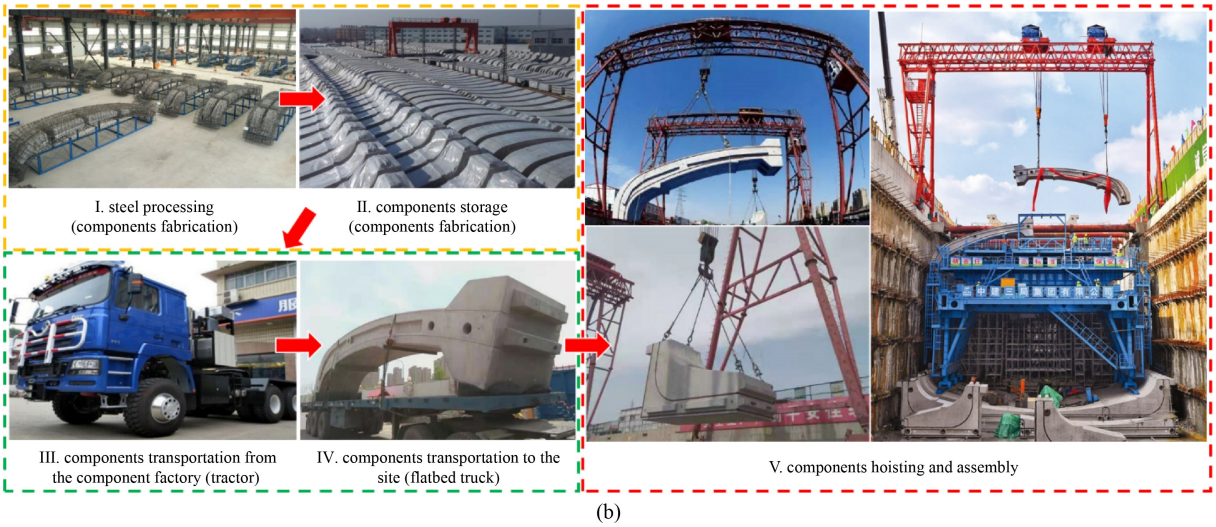

(b)

Fig. 1 Prefabricated subway stations in Changchun, China: (a) five prefabricated subway stations of Changchun Rail Transit Line 2; (b) construction process of the PSSS.

post-casting technology after assembly of prefabricated components, as shown in Fig. 2(a). The prefabricated components are all connected by tongue-and-groove joints, and prestressed steel bars are placed inside the A and B blocks to restrain lateral deformation, as shown in Fig. 2(b). In order to reduce the weight of the components, the lightweight design method is adopted; that is, a different number of thin-walled closed cavities made of lightweight and low-strength materials are set inside each prefabricated component, as shown in Fig. 2(c). The

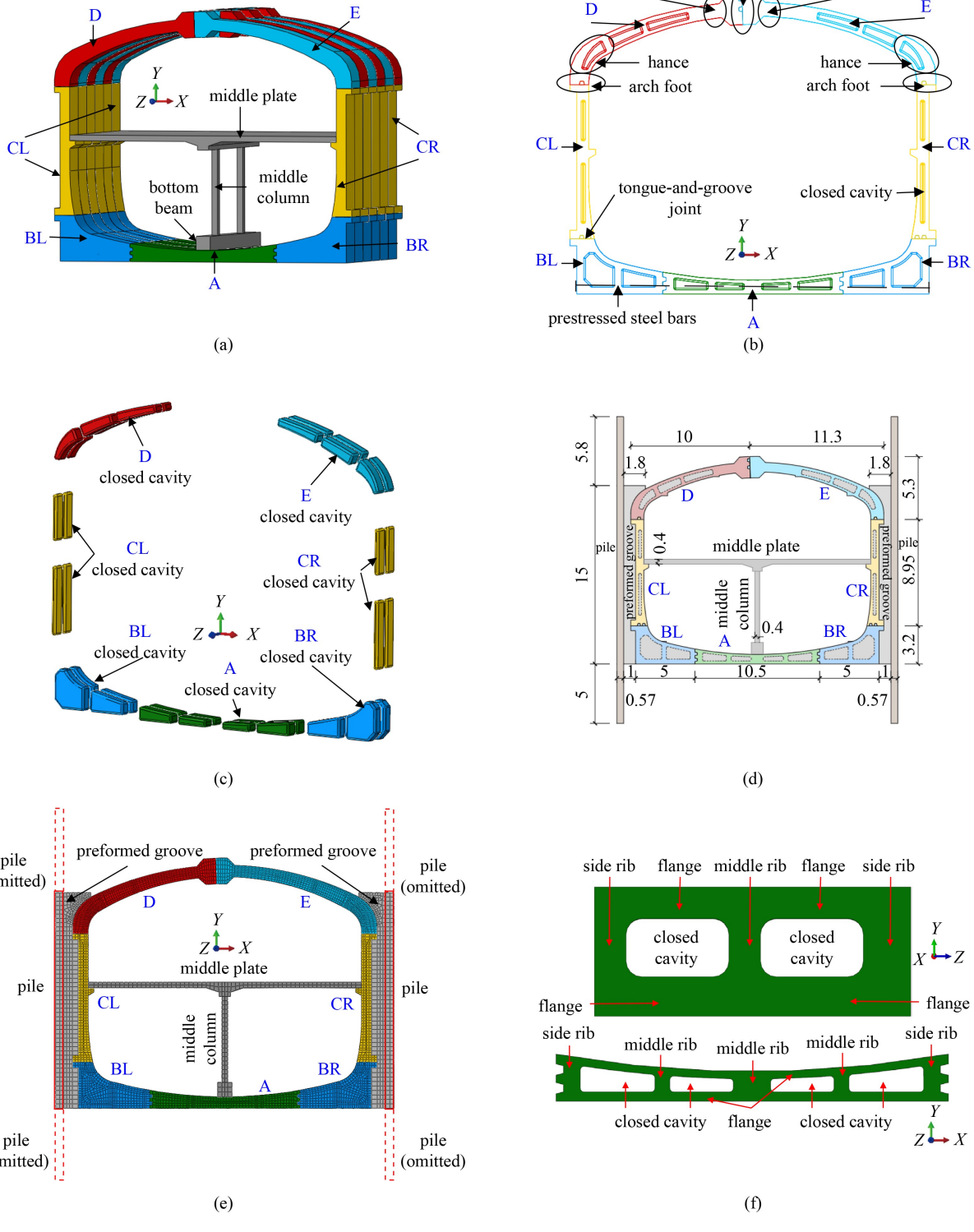

Fig. 2 Notes and details of the PSSS: (a) prefabricated components; (b) perspective view; (c) setting of closed cavities; (d) dimensional drawing (unit: m); (e) 3D FEM; (f) thin-walled component.

enclosure structure is composed of piles and preformed groove. The cross-section of the PSSS system is shown in Fig. 2(d). Since the PSSS is assembled longitudinally based on the standard ring, the standard ring of the PSSS is taken as the research object to establish a 3D FEM using the finite element software ABAQUS. Appropriate element sizes are selected to ensure accuracy and calculation efficiency. The mesh size of prefabricated structure is selected as 0.2 m, that of enclosure structure is 0.5 m, and each component is divided into at least 2 elements in any spatial dimension. In the FEM, the concrete structure is discretized by eight-node linear reduced-integration brick element (C3D8R in ABAQUS), and the reinforcing steel is meshed with three-dimensional two-node truss element (T2D3 in ABAQUS). Therefore, a total of 143433 elements are discretized in the FEM, as shown in Fig. 2(e). In order to facilitate the description of the calculation results below, the key parts of the top arch and the thin-walled components (take A block as an example) are named, as shown in Figs. 2(b) and 2(f).

3.2 Material properties

The mechanical response of concrete is simulated using the concrete damage plastic model (CDP model), which is proposed by Lubliner [54] and improved by Lee and Fenves [55]. The strain softening, stiffness degradation and inelastic strain evolution of concrete are considered in the CDP model. The damage factor is included to reflect the damage mechanism of the concrete under loading. Therefore, the development law of damage and failure of concrete structures can be well simulated by this model. The parameters of the concrete material model are selected based on Chinese Code for Design of Concrete Structures [56], as shown in Table 1. When the tensile damage factor d_t (or compressive damage factor d_c) = 0, the concrete structure has not yet entered the plastic state. When the $0 < d_t$ (or d_c) < 1, the surface of concrete begins to suffer tensile (or compressive) damage. When d_t (or d_c) $\geqslant 1$, the concrete is damaged completely by tension (or compression). The reinforcing steel in the structure is simulated by the ideal elastoplastic model, and embedded into the concrete using the *EMBEDDED ELEMENT command in ABAQUS. It should be noted that relative slip between reinforcing steel and concrete is not considered in the calculation process. The material parameters of the reinforcing steel are presented in Table 2.

3.3 Contact properties

The main contacts in the model are divided into two categories: the first type is the contact of tongue-and-groove joints between prefabricated components. There are seven tongue-and-groove joints in a single-ring prefabricated structure, which are divided into 4 connection types: A−B joint, B−C joint, C−D/E joint, and D−E joint. (Taking D−E joint as an example, as shown in Fig. 3(a), the red area is the contact surface.) The second type is the contact between the prefabricated structure and the enclosure structure, as shown in Fig. 3(b). The above two types of contacts are simulated by the penalty function method [57]. In the normal direction of contact surface, the normal contact compressive stress is transmitted mutually through the contact constraint. The element nodes on the contact surface satisfy Hooke's law and harmonize displacement condition. When the contact surface is separated, the contact constraints are eliminated and the contact surface changes into mutual free surface. The Tangential Contact Shear Stress (TCSS) is also transferred through the contact surface. If the value of the TCSS exceeds the critical value of the shear stress τ_{crit}, slipping will occur at contact surface. Coulomb's friction law is used to simulate the tangential mechanics behaviors and can be expressed as

$$\tau_{crit} = \mu P, \tag{1}$$

where P is the normal contact stress on the interface, and μ is the friction coefficient of the interface. Through the

Table 1 Material parameters of the concrete

components	strength grade	density ($kg \cdot m^{-3}$)	elastic modulus (GPa)	Poisson's ratio	initial compression yield stress (MPa)	limited compression yield stress (MPa)	tensile yield stress (MPa)
A–E	C50	2400	34.5	0.2	12.9	32.4	2.6
middle plate	C40	2400	32.5	0.2	10.7	26.8	2.4
middle column	C50	2400	34.5	0.2	12.9	32.4	2.6
pile	C30	2400	30.0	0.2	8.0	20.1	2.0
preformed groove	C15	2400	22.0	0.2	4.0	10.0	1.2

Note: Compression stiffness recovery parameter = 1.0, tensile stiffness recovery parameter = 0.

Table 2 Material parameters of the reinforcement steel

component	density ($kg \cdot m^{-3}$)	elastic modulus (GPa)	Poisson's ratio	yield stress (MPa)
reinforcement steel	7850	210	0.3	400

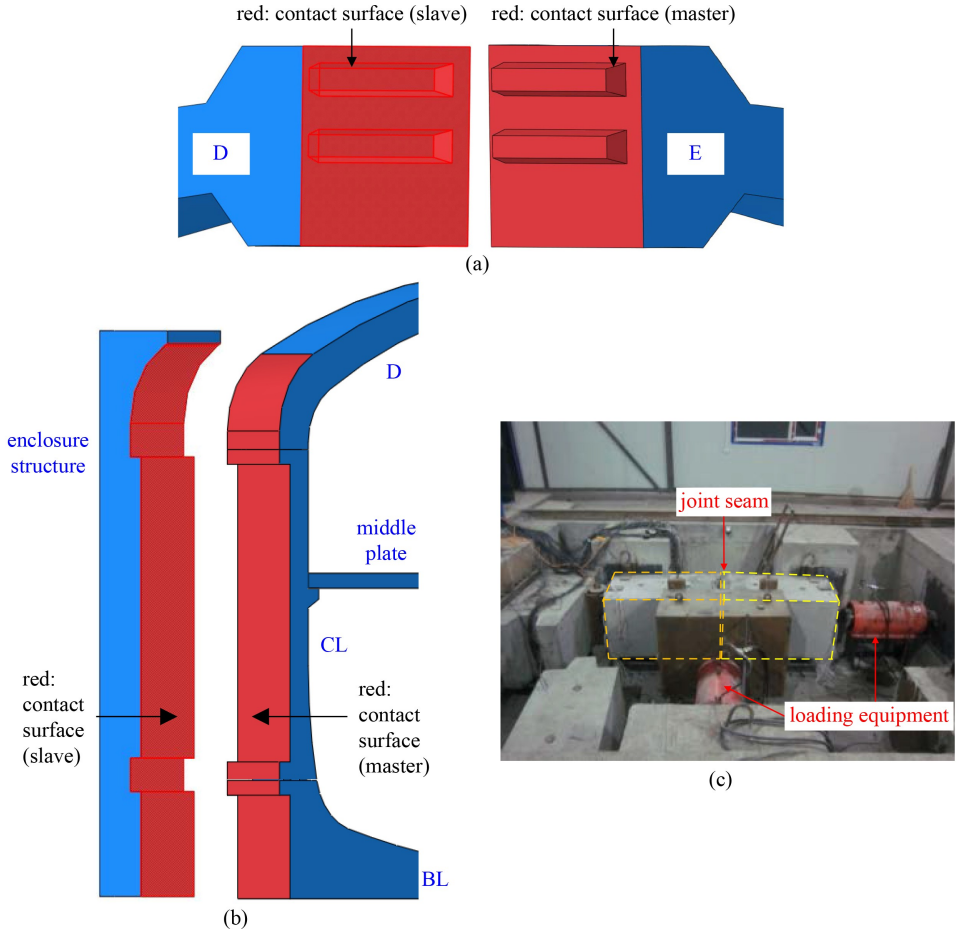

Fig. 3 Schematic diagram of contact surface: (a) tongue-and-groove joint; (b) contact between the PSSS and enclosure structure; (c) performance test tongue-and-groove joint.

test of the performance of the tongue-and-groove joints (as shown in Fig. 3(c)) [58] and related research experience [33–35], the friction coefficient of the contact surface is known to be 0.6.

3.4 Boundary conditions

Firstly, the vertical degree of freedom (*Y*-direction) at the bottom of A and B blocks and the enclosure structure are fixed to simulate the vertical constraints on the structure on the soil cut-off surface in actual engineering. Secondly, the lateral degree of freedom (*X*-direction) at the bottom of A and B blocks are fixed to simulate the prestressed steel bars that enhance the integrity of A and B blocks. Finally, subgrade springs are used to fix the outer lateral degree of freedom (*X*-direction) of the enclosure structure to simulate the lateral restraint of the structure by the soil, as shown in Fig. 4. The stiffness of the subgrade springs can be calculated as

$$k = K \times L \times d, \tag{2}$$

where k is the stiffness of the subgrade springs, K is the coefficient of subgrade reaction, L is the vertical distance between the subgrade springs, and d is the longitudinal distance between subgrade springs in this paper. According to the information provided by the geological survey report, K is 63.4 MPa·m^{-1}. L and d are taken as 0.5 m and 0.3 m according to the actual mesh size of the FEM, respectively. Therefore, the stiffness of the subgrade springs could be calculated to be 9.5×10^6 N·m^{-1}.

3.5 Loading condition setting

The loading process is divided into two steps as follows. Step 1 is to apply gravity to the PSSS. Step 2 is to apply a vertical uniform load with displacement control on the upper surface of D and E blocks, as shown in Fig. 4. That is, the reference point (RF) coupled with the upper surface of the D and E blocks is set directly above the D and E blocks. The vertical displacement is applied at the RF for calculation. After the calculation is complete, the bearing reaction force at the RF can be obtained. The bearing reaction force is divided by the area of the upper surface of the D and E blocks to obtain the vertical uniform load acting on the D and E blocks. The loading condition settings of the PSSS are shown in Table 3. In order to facilitate the analysis and explanation, if the PSSS bears the vertical uniform load of XXX kPa, this

load is uniformly indicated by the working condition code Q-XXX in the following text. For example, the working condition code Q-200 means that the PSSS bears a vertical uniform load of 200 kPa. The reasons for choosing self-weight and vertical uniform load as working condition load are as follows. Firstly, the prefabricated subway station is a large-span structure. In addition, the D-E joint without the protection of the enclosure structure is the weakest part of the entire single-ring PSSS, whose upper part is backfill and lower part is the internal space of the station. Therefore, both the PSSS and the D-E joint are more sensitive to the vertical load.

Table 3 Loading condition setting

analysis step	working condition	load pattern	range of vertical displacement of RF	range of equivalent uniform load
1	G	gravity	0	0
2	Q	gravity + vertical uniform load	0–14 cm	0–590 kPa

4 Analysis of the results

4.1 Mechanical properties

4.1.1 Stress

According to the mechanics of materials, the Mises stress of structure could quickly determine the place where the structure is subjected to greater force, the maximum principal stress of the structure can be used to determine the tensile position of the structure, and the minimum principal stress of the structure can be used to judge the compressive position of the structure. Figure 5(a) shows the stress contours of the PSSS under working condition Q-200 and key points of structural stress. In general, the stress of the upper components (D and E blocks) is significantly greater than that of the lower components (A, B, and C blocks); in particular, the stress distributions at the spandrel and hance of the D and E blocks are more concentrated. The inner side of the hance and the outer side of the spandrel of D and E blocks are mainly subjected to compressive load, and the outer side of the hance and the inner side of the spandrel mainly bear

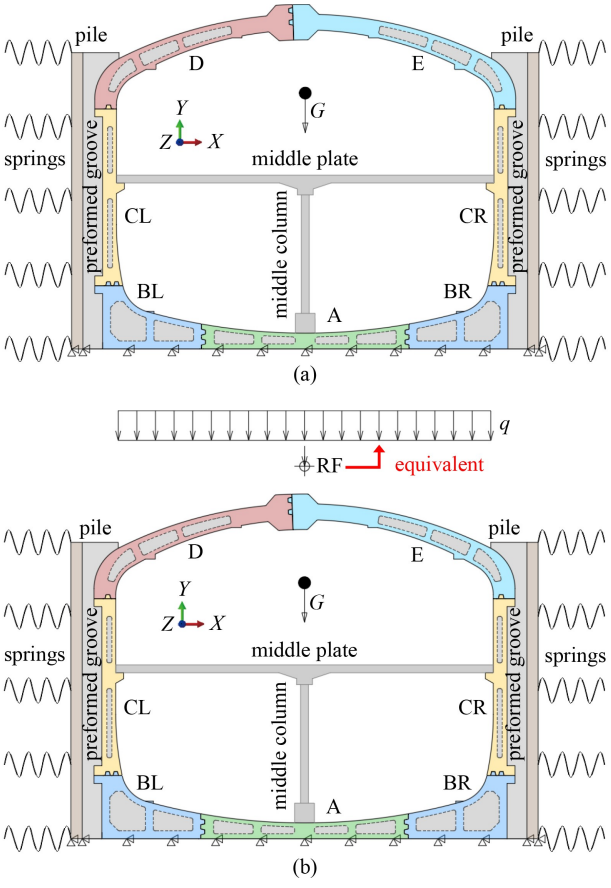

Fig. 4 The process of loading step changes: (a) step 1; (b) step 2.

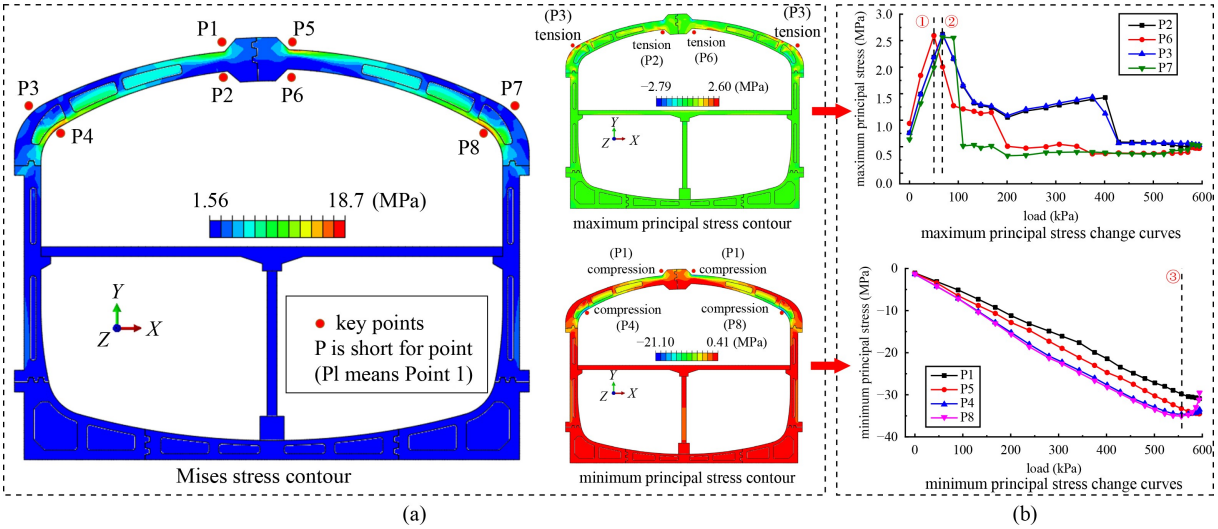

Fig. 5 Stress of the PSSS: (a) stress contours under condition Q-200 (kPa); (b) stress change curves.

tensile load. Figure 5(b) shows the changes of the maximum and minimum principal stresses at key points. At the initial stage of loading, with the uniform increase load with respect to time, the trend of stress changes generally increases linearly. When the structure bears a load of 50 kPa (dotted line ①) and 70 kPa (dotted line ②), the tensile stress at key points reaches the ultimate tensile strength of concrete and then begins to drop rapidly, but finally retains a certain bearing capacity. When the structure bears a load of 560 kPa (dotted line ③), the compressive stress at the hance reaches the extreme value and begins to gradually decrease, and the compressive stress at the spandrel increases with the increase of the load during the loading process. The rapid decline of the stress is caused by the continuous reduction of the bearing capacity of the structure due to the damage occurring in the concrete. When the concrete structure partially enters the plastic stage, the concrete near the damage does not directly lose all its bearing capacity. On the contrary, through continuous local stress adjustment, the concrete near the plastic damage still withstands certain stresses. Besides, the rest of the component away from the damage can also have sustainable and stable bearing capacity.

4.1.2 Internal forces

The internal forces of the PSSS studied in this paper mainly include the axial force, bending moment, and shear force. According to the structural force characteristics and the location of the closed cavity, a total of 19 pairs of the key cross-sections are selected as follows, 1) joints: cross-sections 1, 6 (6'), 9 (9') and 12 (12'); 2) the intermediate location of the closed cavity: cross-sections 3 (3'), 4 (4'), 5 (5'), 7 (7'), 8 (8'), 10 (10'), 11 (11'), 13 (13'), and 14 (14'); 3) the variable cross-sectional position: cross-sections 2 (2'); 4) the slab-column connection: cross-sections 15, 16 (16'), 17 (17'), 18, and 19. The key cross-sections and internal forces values are shown in Fig. 6.

The internal forces can be continuously transmitted inside the PSSS. This indicates that the tongue-and-groove joint could transfer the internal forces between the components normally, and the PSSS connected by the tongue-and-groove joint could naturally bear the load. The D and E blocks are the key parts of the vertical load bearing of the structure. Among them, the vault and spandrel (the cross-section 1 and 2) are respectively the

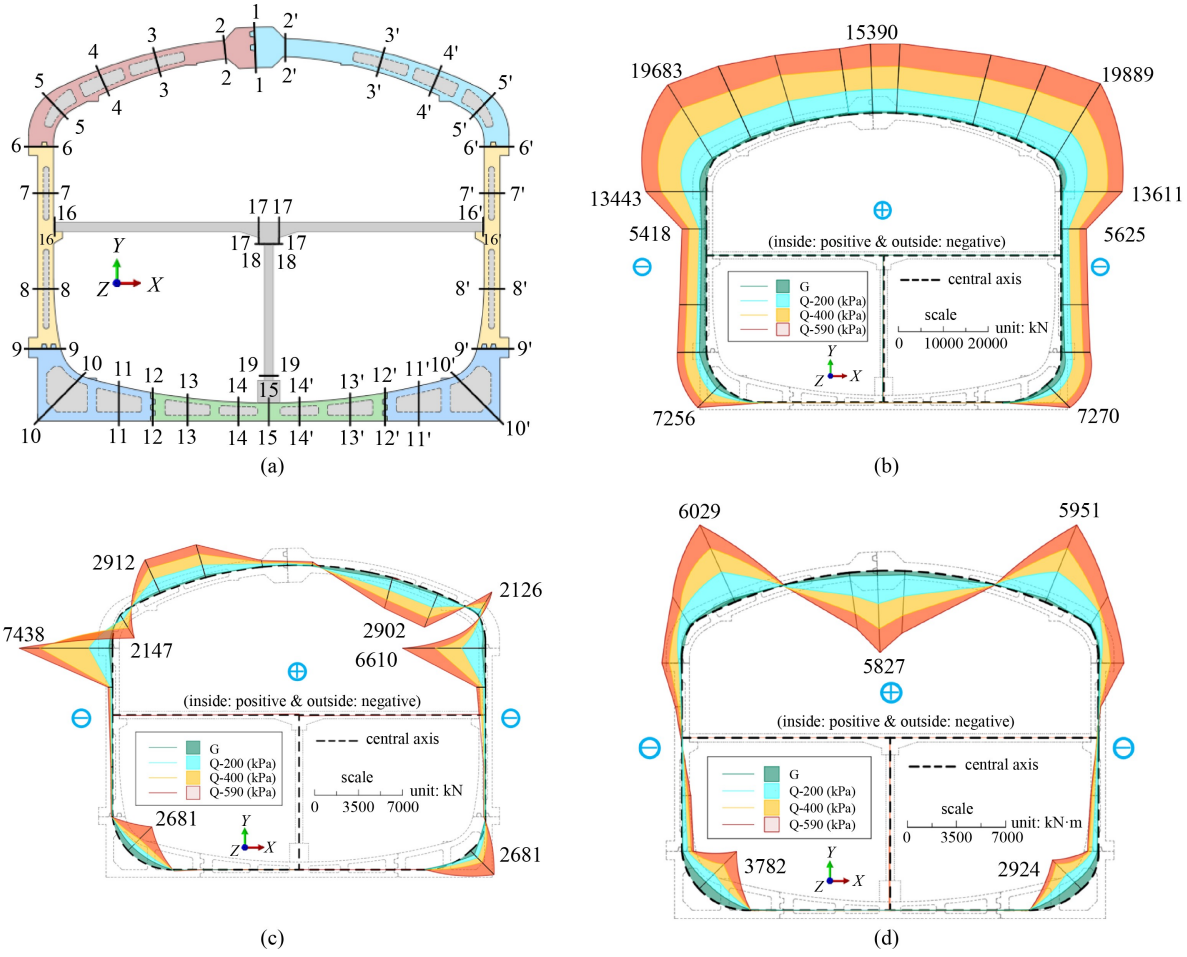

Fig. 6 Internal forces of critical crosssections of the PSSS: (a) distribution of the critical crosssections; (b) axial force; (c) shear force; (d) bending moment.

joint and the variable cross-section, where the internal forces are relatively large and the distribution is relatively concentrated. Moreover, since the hance and arch foot (the cross-section 4–6) with several closed cavities are the intersection area of transmission between the vertical force and the lateral force, the internal forces acting at the hance and arch foot are larger than those of the adjacent position, which is consistent with the above phenomenon reflected by the stress. The internal forces of the C block are greatly reduced, because the enclosure structure bears most of the internal forces transmitted from the arch foot, thereby reducing the internal forces borne by the prefabricated components under the protection of the enclosure structure. The self-weight of the middle slab and column is relatively small, and most of the lateral load of the structure is borne by the enclosure structure and has almost no effect on the middle slab, so the internal forces of the middle slab and column are relatively small. As A and B blocks are laterally constrained by the enclosure structure, and the fixation of prestressed steel bars increases the integrity and rigidity between A and B blocks, the internal forces of A and B blocks are also relatively small. In summary, the vault, spandrel, hance and arch foot are the key areas for the overall forces acting on the PSSS. The enclosure structure is an indispensable and important part of the PSSS, which could significantly reduce the internal forces acting on the structure under its protection, and it works in conjunction with the prefabricated structure to form a common bearing system.

4.2 Deformation analysis

4.2.1 Integral deformation of the structure

The lateral and vertical deformation contours of the PSSS under working condition Q-200 are shown in Fig. 7(a). Under the lateral restraint of the enclosure structure, the expansion of the hance to both sides is accompanied by the inward contraction of the spandrel, and the maximum lateral relative deformation is at the hance (horizontal convergence deformation of hance: expansion to both sides). Meanwhile, the top arch of the structure moves downward as a whole, and the maximum vertical deformation is distributed at vault (vertical deformation of vault: settlement). On the contrary, the deformation of the lower components is much smaller.

Figure 7(b) introduces the change curves of the horizontal convergence deformation of the hance and the vertical deformation of the vault. The deformation trends of the hance and the vault are basically the same. Under self-weight, the structural deformation is relatively small. In the O-P section, the structural deformation increases linearly with the increase of the load, and the PSSS is in a linear elastic stage. In the P-Q section, the structural deformation increases nonlinearly but nearly linearly with the increase of the load. Although the rigidity of the PSSS begins to decrease slowly, it still maintains good integrity. In the Q-R section, as the load continues to increase, the rate of structural increase of deformation gradually becomes faster, and the overall PSSS shows obvious stiffness degradation. In the R-S_2 section, the structural bearing capacity gradually decreases, the structural deformation increases rapidly. The PSSS cannot have the ability to bear a load for the lack of original rigidity. To sum up, the key points of bearing capacity of the PSSS are shown in Table 4.

According to relevant codes and engineering practice experience [16,59], the monitoring limit values of the vertical deformation of the vault and the horizontal

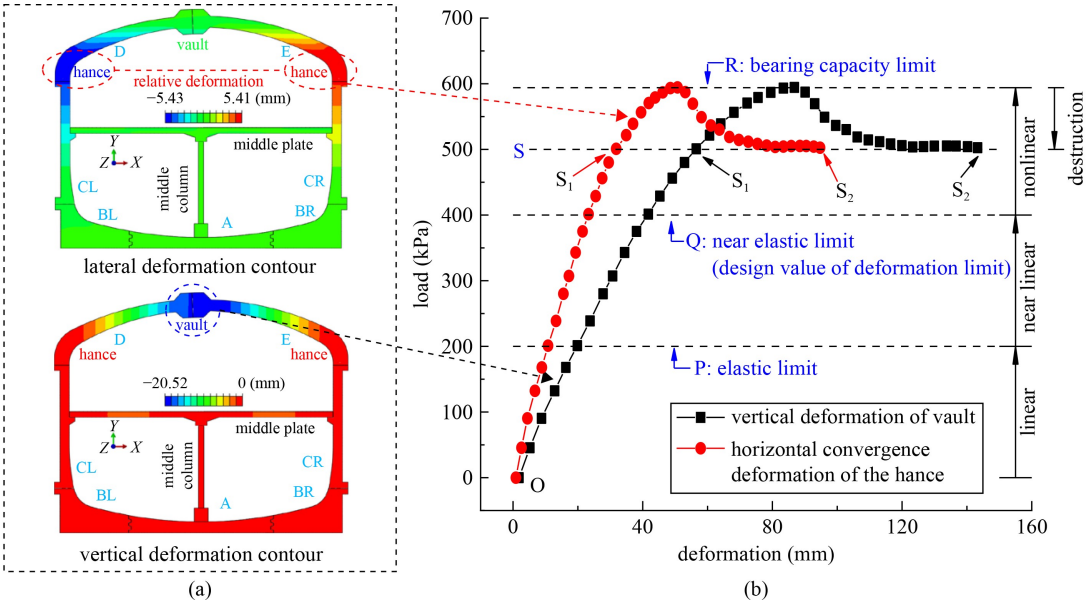

Fig. 7 Deformation of the PSSS: (a) deformation contours under condition Q-200 (kPa); (b) deformation change curves.

convergence of the hance during the construction and operation of the PSSS are 20 and 10 mm, respectively. These values are basically consistent with the elastic limit values corresponding to point P shown in Fig. 7. According to Chinese Code for Design of Concrete Structures [56], when the structural span l is greater than 9 m, the deflection limit of the bending structure is l/300. The span of the top arch of PSSS is 21300 mm, and thus the deflection limit of the top arch structure is 71 mm. However, the code for design of concrete structures is aimed at complete concrete structures, and PSSS has tongue-and-groove joints and the structural rigidity is discontinuous, so the deformation control for the top arch deflection should be more stringent. The near elastic limit value corresponding to point Q shown in Fig. 7 is about 0.6 times the deflection limit of the complete concrete structure. Therefore, it is scientific, rigorous and appropriate to define the Q point as the deformation limit of the PSSS, and a large safety redundancy is reserved.

The deformations of PSSS are monitored in engineering practice [16]. When the 3 m cover soil backfill is completed above the PSSS, the vertical deformation of the vault is 4.60 mm, and the horizontal convergence value of the hance is 3.06 mm, which is far less than the elastic limit value. In general, the actual buried depth of the PSSS is only 3–4 m. According to the calculation of the density of the covering soil as 20 kN·m^{-3}, the actual vertical permanent load of the PSSS is only 60–80 kPa. In extreme cases, considering the equipment, ground vehicle, crowd, and construction loads, the actual vertical load of the PSSS cannot exceed 200 kPa. This shows that during normal construction and operation, the PSSS cannot exceed the elastic limit value, and it cannot reach the design value of deformation limit further. Therefore, this type of PSSS system assembled by thin-walled closed-cavity components meets the design requirements of both bearing and deformation capabilities and has greater safety redundancy.

4.2.2 The opening deformation of tongue-and-groove joints

The COPEN function of the contact in ABAQUS software could monitor the contact state of the two contact surfaces in real time. The squeezed contact surface appears to be closed, and the disengaged contact surface appears to be open. Since the A−B and B−C joints are laterally restrained by the enclosure structure and fixed by the prestressed steel bars and their bearing load is relatively small, the A−B and B−C joints keep relatively closed, and so can be regarded as rigid joints. The opening deformation changes of C−D/E and D−E joints are shown in Fig. 8. Due to the self-rigidity of the C-D/E joints and the protection of the enclosure structure, its opening deformation is relatively small (stable stage). When the load reaches 400 kPa, the C−D/E joints quickly open (rapid opening stage), indicating that the joints stiffness are rapidly degraded. The D−E joint is not protected by enclosure structure, so the joint has a certain opening deformation under its own weight. As the load increases, the opening deformation of the D-E joint continues to increase (opening stage) and the axial force of the top arch structure also increases. When the load reaches 70 kPa, the increasing axial force in turn gradually compresses the joints, and the tongue and groove bite together and become tighter (compaction stage), and then maintain a relatively stable stage (stable

Table 4 The key points of bearing capacity of the PSSS

key point	load (kPa)	vertical deformation of vault (mm)	horizontal convergence deformation of the hance (mm)	design requirement
P (Fig. 7(b))	200	19 (settlement)	11 (expansion to both sides)	elastic limit
Q (Fig. 7(b))	400	41 (settlement)	23 (expansion to both sides)	near elastic limit (design value of deformation limit)
R (Fig. 7(b))	590	86 (settlement)	51 (expansion to both sides)	bearing capacity limit

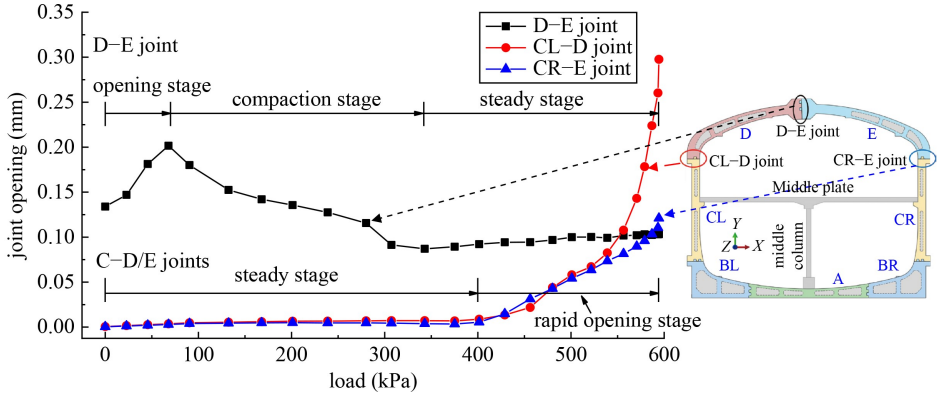

Fig. 8 Change curves of joints opening.

stage). This is because the increase in axial force could improve the bending stiffness of the joint, which is consistent with the phenomenon observed in Li et al.'s test [33]. The opening deformation of the two types of semi-rigid joints, C−D/E and D−E joints, is relatively small, and is much smaller than the maximum opening design allowable value of 10 mm for tongue-and-groove joints [16,58]. This plays important roles in ensuring the overall stability of the PSSS, in the continuous force transmission between components and in the waterproof performance of the structure. Meanwhile, it shows that the tongue-and-groove joint design of the PSSS is reasonable during the loading process, and the opening deformation meets the design requirements.

4.3 Bearing mechanism

Based on the above analysis, the bearing mechanism of the PSSS can be expressed as follows. The top arch structure composed of prefabricated components, D and E blocks, and semi-rigid joints, D−E and C−D/E joints, could be simplified as a three-hinged arch bearing system. The enclosure structure well restrains the deformation of the bottom plate A and B blocks and the side wall C block, and directly or indirectly strengthens the A−B and B−C joints to make them approximately equivalent to rigid joints. As a result, the substructure forms a complete vertical support system for the top three-hinged arch structure system; also, the enclosure structure and C−D/E semi-rigid joints provide horizontal support and restraint for the top three-hinged arch structure system. The schematic diagram of the structural bearing mechanism of the PSSS is shown in Fig. 9. The bearing and force transmission process of the entire PSSS can be summarized as follows.

1) The top arch structure is regarded as a three-hinged arch structure to bear the load and transmit force to the arch foot (red arrow ①→②).

2) The force at the arch foot could be resolved into the superposition of horizontal force and vertical force. The horizontal force is mainly transmitted to the enclosure structure at the arch foot (red arrow ②→③). The vertical force is mainly transmitted downward by C−D/E semi-rigid joint, C block and B-C rigid joint in turn (red arrow ②→④).

3) A and B blocks serve as a solid whole (bottom plate) that bears the upper load and evenly transmits it to the foundation (red arrow ④→⑤).

4.4 Analysis of failure mechanism of single-ring PSSS

4.4.1 Damage evolution of single-ring PSSS

Figures 10 and 11 show the compression and tensile damages of the PSSS, respectively.

For tensile damages, these do not occur on the structure in the process of loading from its own weight to 50 kPa, as shown in Figs. 10(a) and 10(b). Slight tensile damages first appear on the inside of the spandrel in the process of loading from 50 to 590 kPa, and the maximum tensile damage factor d_t is about 0.03. Later, tensile damages occur in turn on the outside of the hance, the enclosure structure at the arch foot, the C−D/E joint and the thin-wall of the closed-cavity near the vault. As the load increases, the tensile damages continue to deepen, and the damage areas rapidly expand. Finally, when the load reaches 590 kPa, serious tensile damages occur at the spandrel, hance, C−D/E joint, and the enclosure structure at the arch foot. The damage zone almost penetrates the entire section, and the maximum tensile damage factor d_t

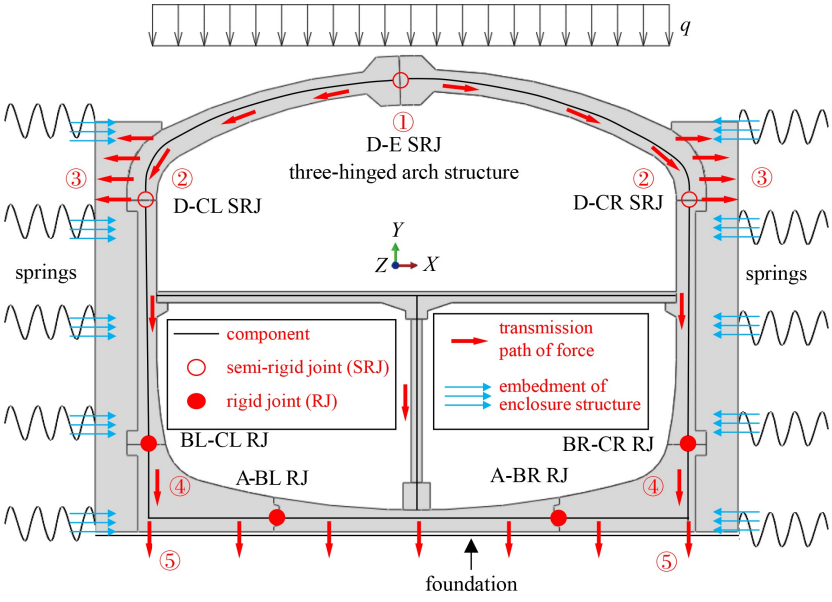

Fig. 9 Schematic diagram of bearing mechanism of the PSSS.

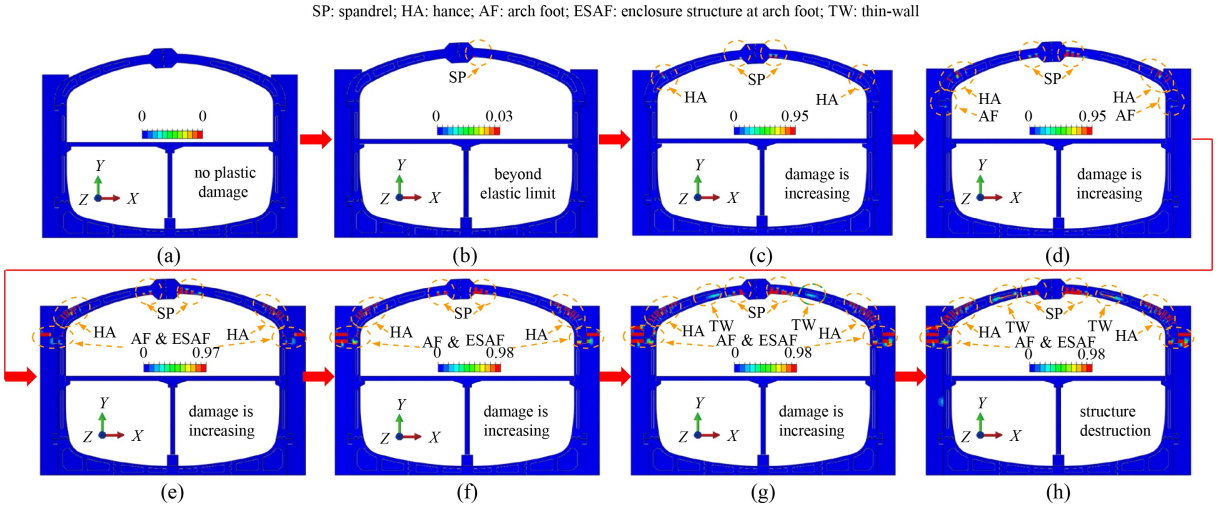

Fig. 10 Contours of tensile damages of the PSSS: (a) G; (b) Q-50 kPa; (c) Q-100 kPa; (d) Q-200 kPa; (e) Q-300 kPa; (f) Q-400 kPa; (g) Q-500 kPa; (h) Q-590 kPa.

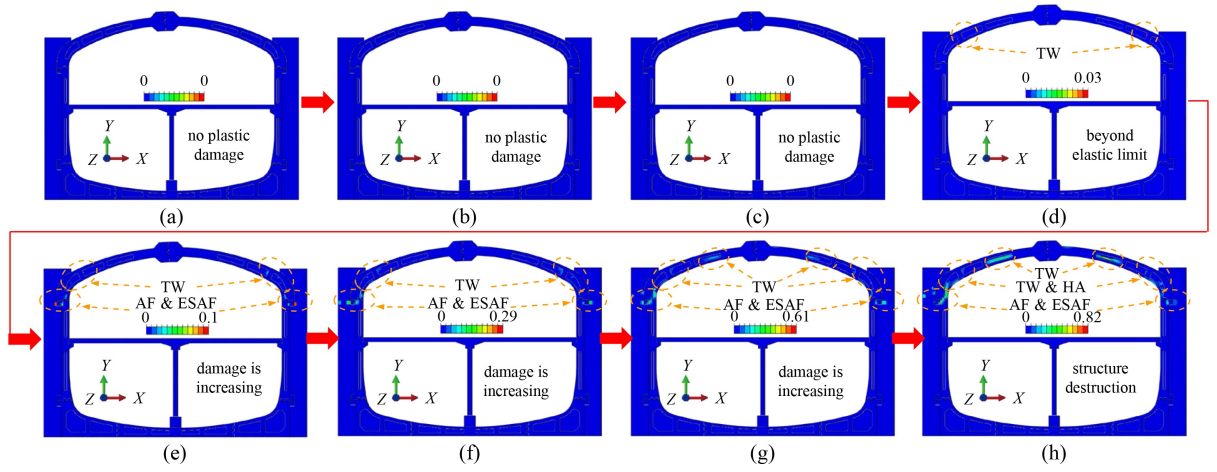

Fig. 11 Contours of compression damages of the PSSS: (a) G; (b) Q-50 kPa; (c) Q-100 kPa; (d) Q-200 kPa; (e) Q-300 kPa; (f) Q-400 kPa; (g) Q-500 kPa; (h) Q-590 kPa.

is about 0.98, as shown in Figs. 10(b)–10(h). When the damage factor reaches this value, it can be considered that the strength of the concrete is completely degraded and operating performance is lost.

For compression damages, these do not occur on the structure in the process of loading from its own weight to 200 kPa, as shown in Fig. 11(a)–11(d). Slight compression damages first appear on the thin-wall of the closed-cavity of the spandrel in the process of loading from 200 to 590 kPa, and the maximum compression damage factor d_c is about 0.03. Afterwards, compression damages occur in sequence on the enclosure structure at the arch foot, the C−D/E joint and the thin-wall of the closed-cavity close to the vault. Finally, when the load reaches 590 kPa, the compression damage factor d_c is about 0.82. But the compression damage distribution areas are more scattered than the tension damage, and the structure with compression damage factor d_c of 0.82 (red area on contours) is even rarer, as shown in Fig. 11(d)–11(h). This phenomenon is consistent with the general rule that concrete structures are resistant to compression but not tension.

4.4.2 Damage analysis of key parts

1) Thin-walled component

Since the forces on the D and E blocks are the most complex and approximately symmetrically distributed, this section takes the D block as an example for analysis. The force transmission paths of the solid component and thin-walled component are shown in Fig. 12, and the summary of the force transmission paths is shown in Table 5. The force transmission paths of the solid components are relatively simple and clear (Fig. 12(a), front view: a→b→c; top view: d→e→f). However, due to the obstruction of the closed-cavity in the thin-walled

Table 5 Statistics of force transmission paths of solid and prefabricated components

structure type	force transmission path	
	front view	top view
solid component (Fig. 12(a))	a→b→c	d→e→f
thin-walled closed-cavity component (Fig. 12(b))	a→b→d, a→c→e	f→g→j, f→h→k, f→i→l

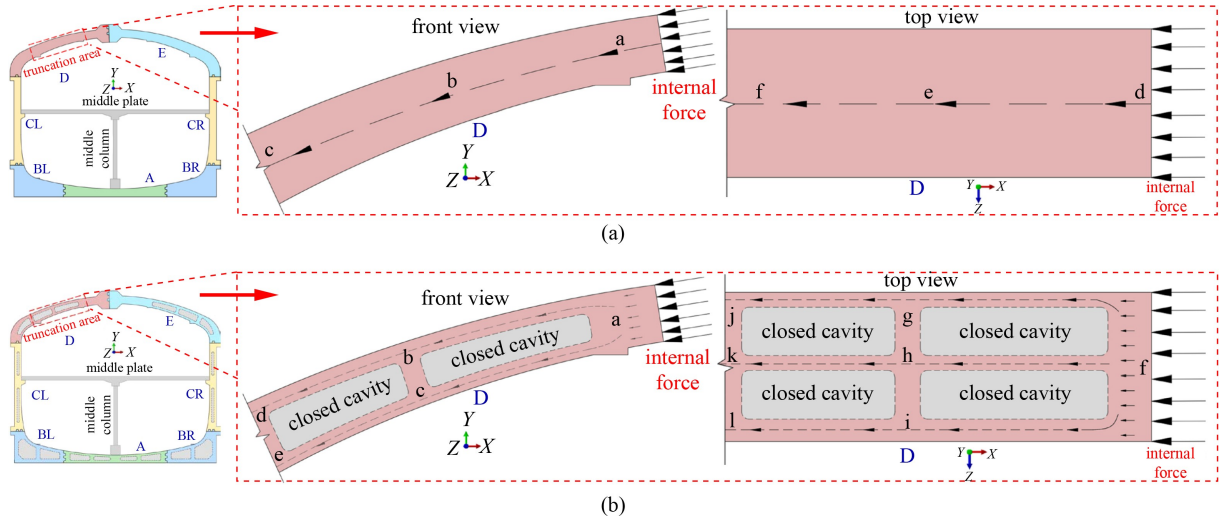

Fig. 12 Force transmission paths of the solid and prefabricated component: (a) solid component; (b) thin-walled component.

components, the force transmission is obviously diverted to the thin-walled areas (Fig. 12(b), front view: a→b→d, a→c→e; top view: f→g→j, f→h→k, f→i→l). The force transmission in the thin-walled areas is extremely complicated, and tension areas, compression areas, and tension and compression mixed areas coexist. Therefore, the thin-walled areas are more prone to stress concentration than the solid structure, which has a greater tendency to experience damage and destruction.

In order to minimize the stress concentration around the thin-walled areas, measures such as round corners of closed-cavities and the double-row closed-cavities are adopted. However, in extreme cases, the stress concentration around the thin-walled areas is inevitable. Therefore, the area around the thin-walled area is one of the weak areas of this type of the PSSS.

2) Tongue-and-groove joint

Figure 13 shows the damage mechanism of the CR−D joint. The inside of the joint is opening and the outside is in compaction. The bending moment and shear force received on the joint are mainly offset by the friction and intercalation between the tongue and the groove, resulting in tensile damage to the root of the tongue and groove, which is consistent with Li et al.'s test [34]. In addition, this tongue-and-groove joint is the main force transmission components of vertical loads, and the contact surface shows continuous compression. As the load continues to increase, insignificant compression damages occur at the contact surface of the joint. Therefore, the stiffness of the joint is mainly controlled by the tensile properties of the concrete at the root of the tongue and the groove.

3) Spandrel and hance

Figure 14 shows the damage mechanism of the spandrel and the hance. The top arch structure is a large-span structure that directly bears vertical loads, and the vault of the middle of the span is not protected by the enclosure structure. Therefore, the D−E joint near the vault is the weakest part of the overall PSSS, and the cross-sectional area of the D−E joint is also designed to be larger. During the bearing process of the PSSS, the internal forces of the D−E joint and the spandrel are similar, but the cross-sectional area of the spandrel is 54.5% smaller than that of the joint, so the spandrel is more prone to damage. The concrete on the outside of the spandrel is mainly damaged under compression, and the concrete on the inside is damaged under tension.

The hance is the component in which vertical and horizontal force transmissions are superimposed, and its forces are relatively large and complex. The deformation of the concrete at the hance tends to cause compression of the closed-cavities, and this deformation is resisted by the middle and side ribs of the thin-walled components. When the load reaches 590 kPa, the outer flange at the hance loses most of its strength, and the damages continue to develop inward to the closed-cavities. Due to the existence of the closed-cavities, the large deformation cannot be resisted by the middle and side ribs alone. Therefore, the strength of the thin-wall degrades rapidly, resulting in a sharp increase in the deformation and

damage at the hance. The concrete on the outside of the hance is mainly damaged under tension, and the concrete on the inside is damaged under compression.

4) Enclosure structure

Most of the lateral deformation of the arch foot and C−D/E joint is restrained by the enclosure structure. The damage mechanism of the enclosure structure is shown in Fig. 15. During the bearing process of the PSSS, the

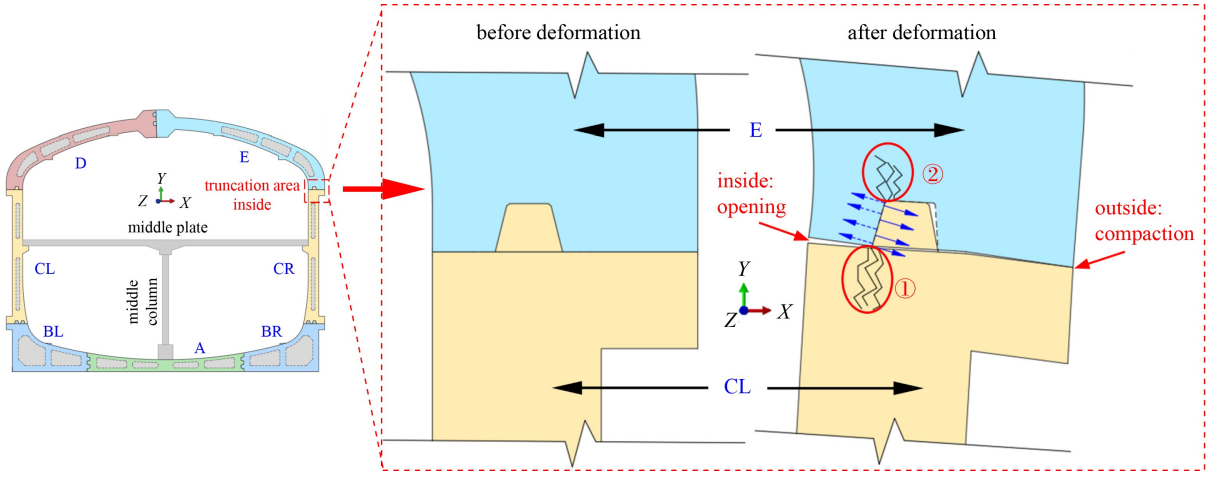

Fig. 13 Schematic diagram of damage mechanism of joint.

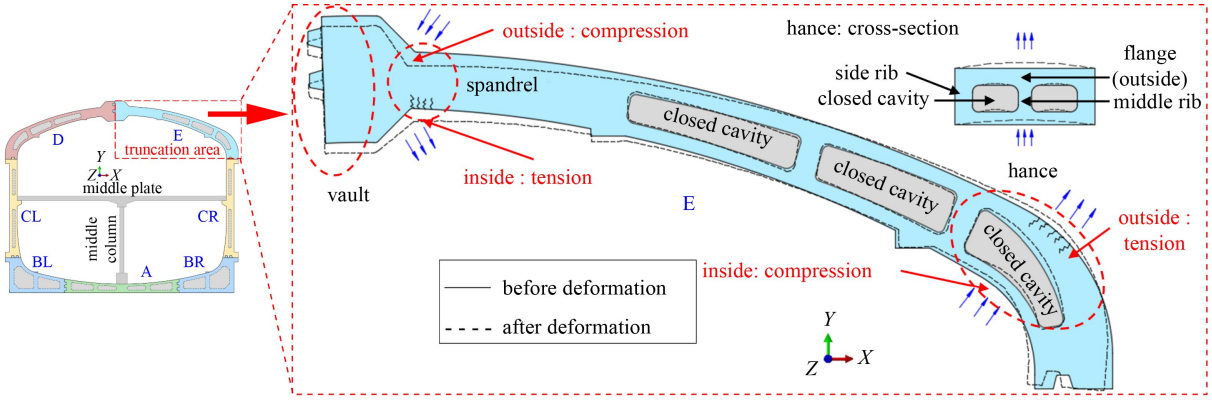

Fig. 14 Schematic diagram of damage mechanism of the spandrel and the hance.

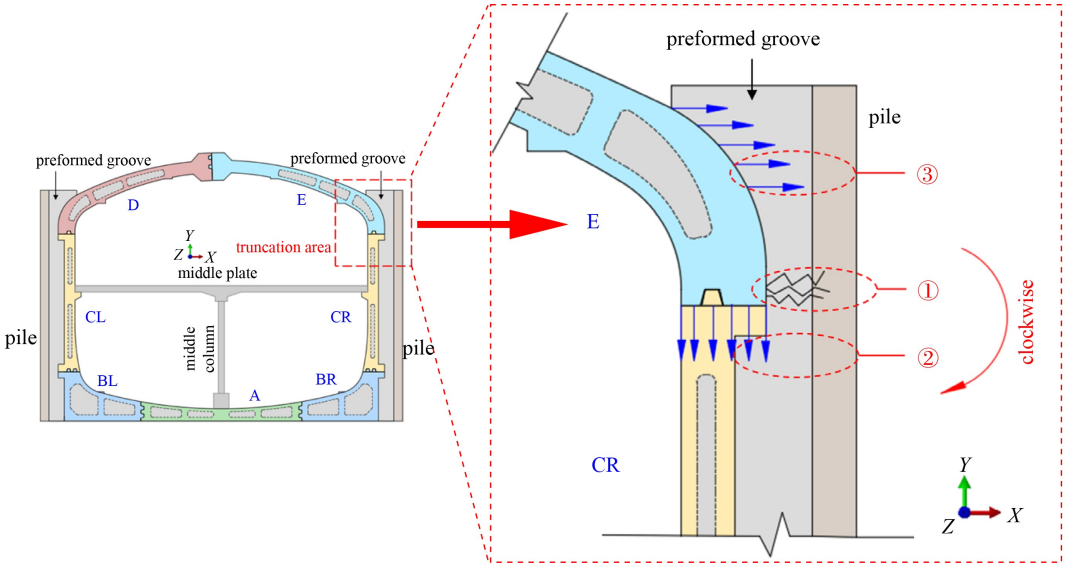

Fig. 15 Schematic diagram of damage mechanism of enclosure structure.

hance is mainly deformed outwards, the E and C blocks move downward as a whole. Meanwhile, the CE joint rotates clockwise to oppress the enclosure structure to make it deform cooperatively with the prefabricated components. Therefore, the positions ② and ③ are subjected to vertical and horizontal compressive loads from the components, respectively, resulting in small compression damages. The concrete at position ① is distributed with severe tensile stress, and the tensile damages almost penetrate the entire section. After increasing the load continuously, the tensile damages continue to extend to the outer piles.

4.4.3 Damage mechanism of single-ring PSSS

According to the load−deformation curves (Fig. 7) and damage contours (Figs. 10 and 11), the failure evolution process of the single-ring PSSS under vertical uniform load is shown in Fig. 16, which can be summarized into the following three stages (see Table 6).

Stage 1: elastic stage. At this stage, the PSSS is basically in the elastic working stage, the structure and joints are not damaged, and the changes between the stress, deformation and load of the components all show linear elastic relations.

Stage 2: elastoplastic stage. It could be divided into the stage of stable development of micro-damage and the stage of rapid development of damage.

1) Stage of stable development of micro-damage. As the load continues to increase, minor damage begins to appear on the spandrel, hance, and the enclosure structure (Fig. 16, Stage 2-a) and gradually develops. At this stage, there is no large-scale damage in the key parts of the overall structure, and most areas of the enclosure structure still retain good strength. Meanwhile, the load-deformation curve at this stage maintains approximately linear change, and it could be considered that the PSSS is still in an approximately elastic stage. The deformations corresponding to the loads of 200 and 400 kPa are defined as the design value of the limit value of construction and operation, and the deformation limit of the PSSS, respectively.

2) Stage of rapid development of damage. As the load continues to increase, the stress concentration areas in the structure become more obvious, and the micro-damages continue to accumulate and develop rapidly. After obvious damages to the enclosure structure at arch foot, the arch foot, hance and spandrel (Fig. 16, Stage 2-b)

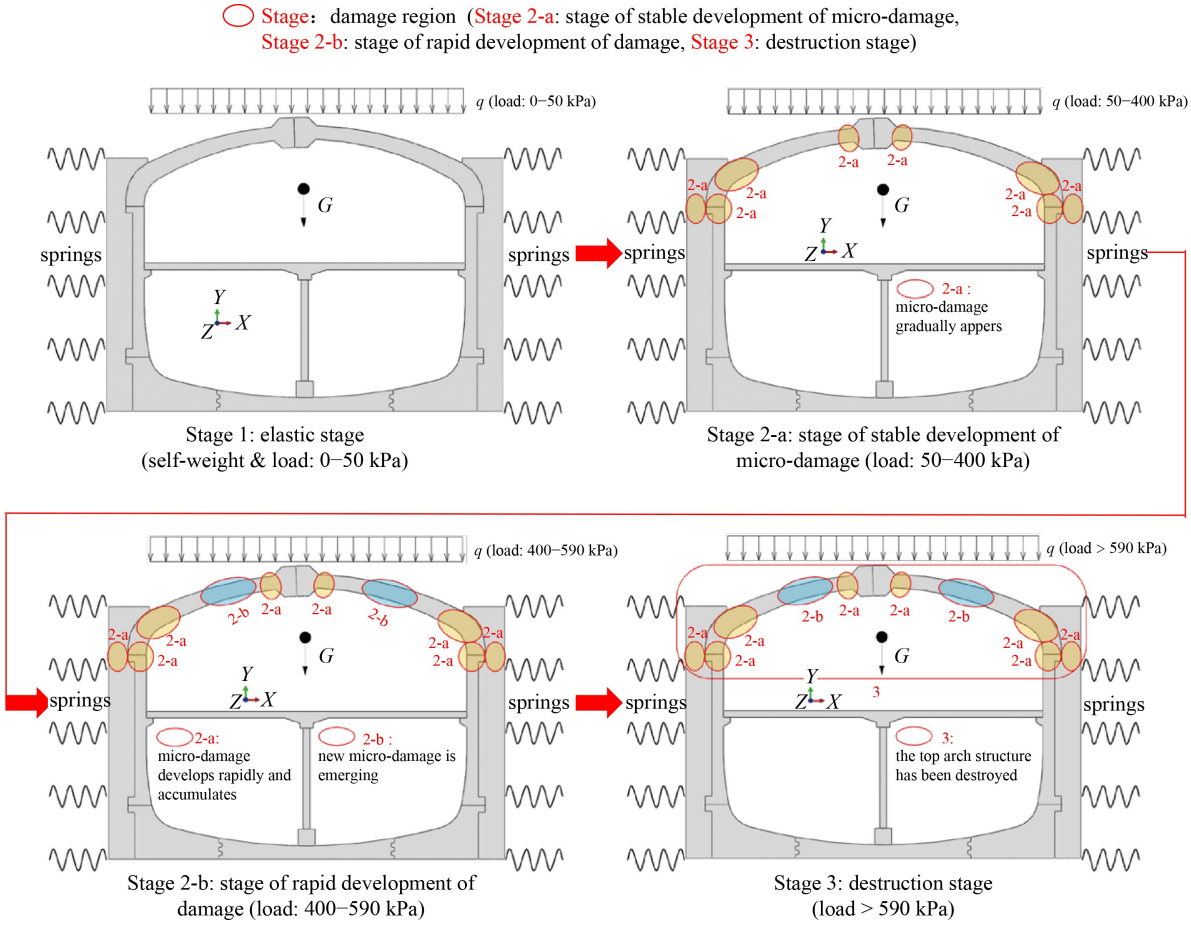

Fig. 16 Schematic diagram of damage mechanism of the PSSS.

Table 6 The failure evolution process of the PSSS

Stage	load (kPa)	vertical deformation of vault (mm)	horizontal convergence deformation of the hance (mm)	opening deformation of tongue-and-groove joints	brief description of structure status
Stage 1: elastic stage	self-wight & 0–50 kPa	0–6	0–3	much less than 10 mm	normal bearing, deformation: linear, no damage
Stage 2: elastoplastic stage					
stage of stable development of micro-damage	50	6	3		normal bearing, start to damage
	50–200	6–19	3–11		normal bearing, deformation: linear, less structural damage
	200	19	11		construction and operation limit values, deformation: change from linear to near linear
	200–400	19–41	11–23		abnormal load, deformation: nearly linear, damage gradually develops
	400	41	23		design value of deformation limit, deformation: change from nearly linear to nonlinear
stage of rapid development of damage	400–590	41–86	23–51		gradually enter the bearing capacity limit, deformation: non-linear, no longer meets the requirements, damage develops rapidly
	590	86	51		bearing capacity limit
Stage 3: destruction stage	>590	>86	>51		structure collapses gradually, deformation increases rapidly

accelerate to failure until the top arch structure is completely destroyed. At this stage, the PSSS has gradually entered the bearing capacity limit, the overall stiffness could not be fully maintained and begins to degrade rapidly. Also, the load-deformation changes appear obviously non-linear, and the structural deformation fails to meet the design requirements.

Stage 3: destruction stage. At this stage, the damages of the arch foot, hance and spandrel develop to a serious degree. The deformation of the top arch structure increases sharply with the increase of load, and its bearing capacity decreases rapidly. The PSSS degenerates from a stable structure to an unstable variable mechanism, which can no longer meet the requirements of safe use; it can be considered that the PSSS enters the destruction stage.

In summary, because the enclosure structure at arch foot is gradually damaged, the horizontal deformation of the arch foot cannot be fixed, the D and E blocks continue to be stressed without the constraints of the enclosure structure. Damages occur in the concrete of the PSSS and continue to expand. The key sections (hance, spandrel and arch foot) of each key components (D and E blocks) yield and fail successively, resulting in a rapid decrease in the overall stiffness of the PSSS, which tends to form an unstable structure, and finally the PSSS loses most of its bearing capacity.

5 Discussion

The PCT is an important technology for the future industrialization and green development of the rail transit industry. It conforms to the national industrial development policy and guidance, and has profound social, technological, and economic benefits. The Changchun PSSS is China's first attempt to apply the PCT to the construction of underground subway stations. In order to realize lightweight and efficient production, hoisting, transportation and assembly of large-scale prefabricated concrete components during construction, and to solve the problem of excessive weight of traditional CIP reinforced concrete structures, prefabricated subway station components designed by thin-walled closed-cavity styles can be creatively adopted. The lightweight benefit of the components is especially significant. Before the lightening, the total weight of each standard ring is 360 t, of which the heaviest component is 65 t and the lightest component is 35.35 t. After lightening, the total weight of each ring is reduced to 300 t, which means an average weight loss of 16.67%. Without greatly reducing the structural mechanics and deformation performance, the design of the thin-walled structure significantly reduces the cost of the production, hoisting, transportation, and assembly of the prefabricated components, as well as material consumption. At the same time, the thin-walled design effectively reduces the heat of hydration of large-volume concrete, and the time for cooling and curing is remarkably shortened, significantly alleviating the cracking phenomenon caused by the large temperature difference in the component, and improving production efficiency and quality. Nevertheless, the lightweight design of components also increases the difficulty of research, design and manufacturing, and the internal force transmission of the thin-wall around the closed-cavity becomes complicated. When making thin-walled closed-

cavity prefabricated components, core molds made of lightweight and low-strength materials are placed inside the steel cage as needed. The core molds must be effectively fixed to the steel cage to resist the buoyancy generated during concrete pouring. Therefore, compared with the solid component manufacturing process, the prefabricated component manufacturing process additionally increases the closed cavity placement, which increases the manufacturing difficulty of the prefabricated component.

In summary, application of the thin-walled closed-cavity type in large-scale underground prefabricated structure is a bold and effective innovative attempt. Through scientific and reasonable closed-cavity setting and thin-walled structure design, the appropriate reduction of structural bearing performance and the weight reduction and efficiency enhancement of components achieve a good balance between economy and safe use. Application of PCT achieves good comprehensive benefits and can provide new design ideas for similar project construction.

6 Conclusions

The present study systematically investigates the nonlinear mechanics and deformation performance of the new single-ring thin-walled PSSS using 3D numerical models. Moreover, the force transmission paths and bearing mechanism of the PSSS are analyzed in detail. The failure evolution mechanism of the PSSS under the ultimate bearing condition is discussed, based on its mechanics, deformation and failure characteristics. According to the results of this study, the following conclusions can be drawn.

1) Spandrel, hance, and arch foot are the key areas that affect the bearing characteristics of the new PSSS. The thin-walled area of the prefabricated component is subjected to mixed forces under tension and compression, and its mechanical response is complex. The tongue-and-groove joints have good connection performance, and can effectively transmit the internal force between the components to make them coordinately deformed, thus enhancing the integrity and stability of the PSSS.

2) The enclosure structure is an indispensable part of the new PSSS system. The enclosure structure can significantly reduce the internal force of the structure under its protection, effectively decrease the horizontal deformation of the top arch structure and limit the opening deformation of the tongue-and-groove joints, so that the PSSS can meet the design requirements of stable and reliable force transmission and safe and controllable deformation.

3) The bearing system of the PSSS is mainly composed of prefabricated components connected by tongue-and-groove joints and enclosure structure. Among them, the top arch structure is a three-hinged arch system to bear the load. The enclosure structure and the substructure ensure the stability of the overall structure as the horizontal and vertical support systems of the three-hinged arch structure, respectively.

4) Under vertical uniform loads, the PSSS experiences the elastic stage, the elastoplastic stage and the destruction stage successively. The initial yield of the structure appears in the spandrel, hance, arch foot, and the enclosure structure at the arch foot. With the expansion of the plastic damage areas in these parts, the PSSS gradually develops into an unstable structure, which in turn leads to the loss of bearing capacity.

5) The new thin-walled PSSS has good bearing performance and large safety redundancy under the design load, and fully meets the design and safe use requirements. The thin-walled closed-cavity design of the existing prefabricated components achieves a good balance between structural safety and economy, and provides good comprehensive benefits.

Acknowledgements The authors gratefully acknowledgement the financial support provided by the National Key R&D Program of China (Nos. 2017YFC0805403 and 2019YFC1509704), and the National Natural Science Foundation of China (Grant Nos. 41877218 and 42072308).

References

1. Badir Y F, Kadir M R A, Hashim A H. Industrialized building systems construction in Malaysia. Journal of Architectural Engineering, 2002, 8(1): 19−23
2. Zhao C, Zhang Z, Wang J, Wang B. Numerical and theoretical analysis on the mechanical properties of improved CP-GFRP splice sleeve. Thin-walled Structures, 2019, 137: 487−501
3. Wang Z, Shen H, Zuo J. Risks in prefabricated buildings in China: Importance-performance analysis approach. Sustainability, 2019, 11(12): 3450
4. Liu G, Gu T, Xu P, Hong J, Shrestha A, Martek I. A production line-based carbon emission assessment model for prefabricated components in China. Journal of Cleaner Production, 2019, 209: 30−39
5. Frosch R J, Li W, Jirsa J O, Kreger M E. Retrofit of non-ductile moment-resisting frames using precast infill wall panels. Earthquake Spectra, 1996, 12(4): 741−760
6. Kesner K, Billington S L. Investigation of infill panels made from engineered cementitious composites for seismic strengthening and retrofit. Journal of Structural Engineering, 2005, 131(11): 1712−1720
7. Boyd N, Khalfan M M A, Maqsood T. Off-site construction of apartment buildings. Journal of Architectural Engineering, 2013, 19(1): 51−57
8. Wan Omar W M S, Doh J H, Panuwatwanich K, Miller D. Assessment of the embodied carbon in precast concrete wall panels using a hybrid life cycle assessment approach in Malaysia. Sustainable Cities and Society, 2014, 10: 101−111

9. Steinhardt D A, Manley K. Adoption of prefabricated housing—The role of country context. Sustainable Cities and Society, 2016, 22: 126−135
10. Kasperzyk C, Kim M K, Brilakis I. Automated re-prefabrication system for buildings using robotics. Automation in Construction, 2017, 83: 184−195
11. Lacey A W, Chen W, Hao H, Bi K. Structural response of modular buildings—An overview. Journal of Building Engineering, 2018, 16: 45−56
12. Ferdous W, Bai Y, Ngo T D, Manalo A, Mendis P. New advancements, challenges and opportunities of multi-storey modular buildings—A state-of-the-art review. Engineering Structures, 2019, 183: 883−893
13. Tao L, Ding P, Lin H, Wang H, Kou W, Shi C, Li S, Wu S. Three-dimensional seismic performance analysis of large and complex underground pipe trench structure. Soil Dynamics and Earthquake Engineering, 2021, 150: 106904
14. Deng Z, Liang N, Liu X, de la Fuente A, Lin P, Peng H. Analysis and application of friction calculation model for long-distance rock pipe jacking engineering. Tunnelling and Underground Space Technology, 2021, 115: 104063
15. Su H, Liu W, Liu F. Preliminary ideas of the metro station constructed by shield tunneling method combined with prefabricated method. Applied Mechanics and Materials, 2014, 580–583: 1013–1018
16. Yang X, Lin F. Prefabrication technology for underground metro station structure. Tunnelling and Underground Space Technology, 2021, 108: 103717
17. Freas G C, Shoemaker M J, Ervin D. Precast prestressed underground fuel storage tanks in Adak, Alaska. PCI Journal, 1985, 30(4): 52−63
18. Yurkevich P. Developments in segmental concrete linings for subway tunnels in Belarus. Tunnelling and Underground Space Technology, 1995, 10(3): 353−365
19. Fukayama K, Shinagawa K. Design-construction of circular roof for underground reservoir using precast concrete beams. PCI Journal, 1998, 43(5): 46−54
20. Scott J, Nelson C, Middleton L, Reneson D, Stehler D. Curved precast concrete panels carve out underground library at University of Minnesota. PCI Journal, 2000, 45(1): 40−49
21. Chen J, Mo H. Mechanical behavior of segment rebar of shield tunnel in construction stage. Journal of Zhejiang University-Science A, 2008, 9(7): 888−899
22. He C, Wang B. Research progress and development trends of highway tunnels in China. Journal of Modern Transportation, 2013, 21(4): 209−223
23. Zhu H, Huang B, Li X, Hashimoto T. Unified model for internal force and deformation of shield segment joints and experimental analysis. Chinese Journal of Geotechnical Engineering, 2014, 36: 2153–2160 (in Chinese)
24. Zhuang X, Zhu H, Augarde C. An improved meshless Shepard and least squares method possessing the delta property and requiring no singular weight function. Computational Mechanics, 2014, 53(2): 343−357
25. Yang X, Han Y. Closed cavity thin-wall components design for prefabricated underground subway structures. In: Geo-risk Conference, 2017: Reliability-Based Design and Code Developments. 194–205
26. Yang X, Huang M, Lin F. Experimental study on flexural bearing capability of short grouted single mortise-tenon joints in prefabricated metro station structure. China Civil Engineering Journal, 2020, 53: 57–64 (in Chinese)
27. Yang X, Lin F, Huang M. Research on flexural bearing capability of long grouted single mortise-tenon joints for prefabricated metro station structures. China Civil Engineering Journal, 2020, 53: 111–118+128 (in Chinese)
28. Ding P, Tao L, Yang X, Zhao J, Shi C. Three-dimensional dynamic response analysis of a single-ring structure in a prefabricated subway station. Sustainable Cities and Society, 2019, 45: 271−286
29. Ding P, Tao L, Yang X, Zhao J, Shi C, An S. Force transfer and deformation mechanism of single ring structure of prefabricated subway station. Journal of Southwest Jiaotong University, 2020, 55: 1076–1084+1110 (in Chinese)
30. Ding P, Tao L J, Shi C, Wu X W, Wu S, Li S C. Study on horizontal and vertical seismic response of single-arch and large-span prefabricated subway station. In: 14th International Congress on Rock Mechanics and Rock Engineering. Foz do Iguaçu: ISRM, 2020: 772−2779
31. Tao L, Ding P, Shi C, Wu X, Wu S, Li S. Shaking table test on seismic response characteristics of prefabricated subway station structure. Tunnelling and Underground Space Technology, 2019, 91: 102994
32. Tao L, Ding P, Yang X, Lin P, Shi C, Bao Y, Wei P, Zhao J. Comparative study of the seismic performance of prefabricated and cast-in-place subway station structures by shaking table test. Tunnelling and Underground Space Technology, 2020, 105: 103583
33. Li Z, Li S, Su H. Study on the bending stiffness for double tenon-groove joints of metro station constructed by using prefabricated structure. China Civil Engineering Journal, 2017, 50: 14–18 (in Chinese)
34. Li Z, Su H, Lu S, Wang C, Xu X. Experimental study on flexural mechanical properties of the double tenon groove joints of prefabricated subway station. China Civil Engineering Journal, 2017, 50: 28–32 (in Chinese)
35. Li Z, Li K, Lu S, Su H, Wang C. Experimental study on stress evolution rule of double tenon-groove joints for prefabricated metro station structure. China Railway Science, 2018, 39: 15–21 (in Chinese)
36. Du X, Liu H, Lu D, Xu C, Luo F, Li S. Study on seismic performance of sidewall joints in assembled monolithic subway station. China Civil Engineering Journal, 2017, 50: 38–47 (in Chinese)
37. Du X, Liu H, Xu C, Jin L, Luo F, Li S. Experimental study on seismic performance of precast column in assembled monolithic subway station under different axial compression ratio. Journal of Building Structures, 2018, 39: 11–19 (in Chinese)
38. Liu H, Yan Q, Du X. Seismic performance comparison between precast beam joints and cast-in-place beam joints. Advances in Structural Engineering, 2017, 20(9): 1299−1314
39. Liu H, Han Q, Bai Y, Xu C, Du X. Connection performance of

restrained deformed grouted sleeve splice. Advances in Structural Engineering, 2018, 21(3): 488−499
40. Lu L, Han S, Chen Z, Wang G, Wang Y, Zhao K. Study on bending performance of prefabricated square pile with socket and spigot joint. Journal of Building Structures, 2018, 39: 153–161 (in Chinese)
41. Jin J, Jia J, Huang W. Structural design and construction key technology of precast arch roof plate in subway station. Building Construction, 2020, 42: 1513–1515 (in Chinese)
42. Chu M, Liu J, Hou J, Qiu G, Liu M, Wang G. Experimental study on mechanical behaviors of concrete shear wall with precast two-way hollow slabs. Journal of Building Structures, 2017, 38: 32–40 (in Chinese)
43. Xiong C, Chu M, Liu J, Sun Z. Shear behavior of precast concrete wall structure based on two-way hollow-core precast panels. Engineering Structures, 2018, 176: 74−89
44. Gu Q, Dong G, Ke Y, Tian S, Wen S, Tan Y, Gao X. Seismic behavior of precast double-face superposed shear walls with horizontal joints and lap spliced vertical reinforcement. Structural Concrete, 2020, 21(5): 1973−1988
45. Lee D H, Park M K, Oh J Y, Kim K S, Im J H, Seo S Y. Web-shear capacity of prestressed hollow-core slab unit with consideration on the minimum shear reinforcement requirement. Computers and Concrete, 2014, 14(3): 211−231
46. Park M K, Lee D H, Han S J, Kim K S. Web-shear capacity of thick precast prestressed hollow-core slab units produced by extrusion method. International Journal of Concrete Structures and Materials, 2019, 13(1): 7
47. Nguyen T N H, Tan K H, Kanda T. Investigations on web-shear behavior of deep precast, prestressed concrete hollow core slabs. Engineering Structures, 2019, 183: 579−593
48. El-Remaily A, Tadros M K, Yamane T, Krause G. Transverse design of adjacent precast prestressed concrete box girder bridges. PCI Journal, 1996, 41(4): 96−107
49. Attanayake U, Aktan H. First-generation ABC system, evolving design, and half a century of performance: Michigan side-by-side box-beam bridges. Journal of Performance of Constructed Facilities, 2015, 29(3): 04014090
50. Barbieri D M, Chen Y, Mazzarolo E, Briseghella B, Tarantino A M. Longitudinal joint performance of a concrete hollow core slab bridge. Transportation Research Record: Journal of the Transportation Research Board, 2018, 2672(41): 196−206
51. Ou Y, Chiewanichakorn M, Aref A J, Lee G C. Seismic performance of segmental precast unbonded posttensioned concrete bridge columns. Journal of Structural Engineering, 2007, 133(11): 1636−1647
52. Kim D H, Moon D Y, Kim M K, Zi G, Roh H. Experimental test and seismic performance of partial precast concrete segmental bridge column with cast-in-place base. Engineering Structures, 2015, 100: 178−188
53. Zhu L, Zhang B, Guo Y. Cost analysis and countermeasure research of prefabricated stairs on site. Build Structure, 2019, 49: 539–544 (in Chinese)
54. Lubliner J, Oliver J, Oller S, Oñate E. A plastic-damage model for concrete. International Journal of Solids and Structures, 1989, 25(3): 299−326
55. Lee J, Fenves G L. Plastic-damage model for cyclic loading of concrete structures. Journal of Engineering Mechanics, 1998, 124(8): 892−900
56. GB 50010-2010. Code for Design of Concrete Structures. Beijing: China Architecture & Building Press, 2010 (in Chinese)
57. Abaqus. Version 6.14. Documentation. Providence, RI: Dassault Systèmes, 2015
58. Yang X, Shi Z, Lin F. Influence of geometrical parameters on performance of grouted mortise and tenon joints for application in prefabricated underground structures. Advances in Civil Engineering, 2019, 2019: 1−14
59. GB 50911-2013. Code for monitoring measurement of urban rail transit engineering. Beijing: China Architecture & Building Press, 2013 (in Chinese)